Yadong Zhou, An Dengb, Jiyu Fu
Modelling electro-osmosis-surcharge preloading combined consolidation of unsaturated soils
Computers and Geotechnics, 2019; 114:103145-1-103145-13

Modelling electro-osmosis–surcharge preloading combined consolidation of unsaturated soils

Yadong Zhou[a], An Deng[*b], and Jiyu Fu[a]

[a] Tianjin Key Laboratory of Soft Soil Engineering Characteristics and Engineering Environment

Tianjin Chengjian University

Tianjin 300384, China

*Corresponding author

[b]School of Civil, Environmental and Mining Engineering

The University of Adelaide

Adelaide SA 5000, Australia

E-mail addresses: zyd476300@126.com (Yadong Zhou). an.deng@adelaide.edu.au (An Deng). fcszji201001@163.com (Jiyu Fu)

Abstract: Electro-osmosis often dewaters soils into unsaturated conditions. The unsaturated conditions invalidate electro-osmosis models that are developed by assuming presence of full saturation throughout. The unsaturated condition causes non-negligible influences on soil geomechanical properties and its consolidation behaviour, and should be accounted for. This study presents a numerical model, UEC2, of simulating electro-osmosis–surcharge preloading combined consolidation considering varied degree of saturation of soil. Model UEC2 is able to capture nonlinear changes of soil properties, time-dependent loading and instantaneous pore air compression. This model was validated against laboratory test results, and was applied to varied test examples in order to assess evolvement of unsaturated conditions and its effect on consolidation.

Keywords: Large-strain consolidation; electro-osmosis; surcharge preloading; unsaturated; seepage; nonlinear

1. Introduction

Electro-osmosis is the motion of liquid in porous media under influence of electric field. When subjected to electro-osmosis, pore water is driven, under an ionic current, to travel towards the electric terminals, enabling a flow independent on particle size. A competitive advantage of electro-osmosis is the success of removal of pore water of down to the nano-scale, thus enabling the finest dewatering. This is advantageous over the other consolidating methods e.g. surcharge preloading which is very time-consuming when applied to less permeable soils. Electro-osmosis applied to the porous media has been shown to be successful in generating pore water flow through a less permeable area or a clogging smear zone [1-5].

Although electro-osmosis is showing great trait in porous media dewatering, challenges remain with respect to accurately predicting rate of flow, soil deformation and resulting energy consumption. Earlier studies [6-10] have developed consolidation models from the largely idealised perspective of full saturation. This assumption helps simplify model development, and is acceptable for soils of relatively high moisture contents [11], or soil layers with an open boundary at anodes [12]. However, if the soils have been dewatered to below the liquid limit, or the boundary at anodes is closed, as is required in many scenarios, the soil layers become partially saturated, mainly caused by negative pore water pressure, throughout the dewatering process [12]. The emerging unsaturated condition invalidates the assumption of full saturation in electro-osmosis and therefore restricts models suitability.

The partially saturated condition was considered in the model developed by Wang *et al.* [13]. Their model however is subject to conditions of constant and homogeneous soil properties, and therefore is restricted to small strain consolidation or thin layers where linear Darcy's flow occurs. Large-strain deformation of up to 23% has been recorded in consolidating fine-grained soils [1]. Large-strain deformation is significant in dynamically influencing the media's consolidation properties (e.g., hydraulic conductivity, void ratio, electrical resistivity and electro-osmotic conductivity), in particular when the soils become unsaturated [1, 14]. Numerically, the large-strain consolidation in unsaturated conditions was examined by Yuan and Hicks [15]. However, it is unclear whether or not their model accounts for the full dewatering process of from the saturated to unsaturated conditions. Identifying this transition helps gauge the state of water saturation and apply the suitable algorithms (i.e., saturated vs. unsaturated). In addition it is unclear whether their model is validated against unsaturated scenarios or not. Zhou *et al.* [16] developed a one-dimensional electro-osmotic consolidation model for unsaturated soils, called UEC1. Model UEC1 is able to capture the saturation-to-unsaturation transition, and to account for the soil layer large strain, nonlinear changes in soil properties and varied degree of saturation. Their model is limited to a sole electro-osmosis process and cannot simulate the electro-osmosis–surcharge preloading combined process. All of the above elements, including the unsaturated conditions, property changes, nonlinear Darcy's flow, and the effect of surcharge preloading, are predictable or approachable

78 within engineering accuracy once the factors that govern them are understood. These
79 elements can be integrated into a computational program to refine the approximation
80 of consolidation process.
81
82 In this paper, a numerical model for one-dimensional consolidation considering
83 saturation variation of soil layer subjected to the electro-osmosis–surcharge
84 preloading method, called UEC2, is presented. The UEC2 model is the next step of
85 UEC1 and has all the capabilities that model UEC1 has. In addition, model UEC2 is
86 developed to account for time-dependent loading, instantaneous pore compression
87 associated with the combined effects of electro-osmosis and surcharge preloading.
88 The UEC2 model was examined and validated against laboratory test results, and was
89 applied to some interesting example problems in order to optimise the consolidation.
90
91 **2. MODEL DESCRIPTION**
92 ***2.1 Geometry***
93 The model geometry of the electro-osmosis–surcharge preloading consolidation is
94 presented in Figure 1. A soil stratum has an initial height H_0 and is subjected to
95 initial vertical load q_0. The stratum is divided equally in the horizontal direction into
96 R_j elements. Each element has a thickness $L_0 = H_0 / R_j$. An Eulerian coordinate
97 system, *z*, coincides with the bottom of the stratum, with a positive direction against
98 the gravity. The initial elevation of the central node of element *j* is $z_{0,j}$. At time $t \geq 0$,
99 a combination of direct current voltage V_m^t and vertical load increment Δq^t is

applied to the stratum. The anode and cathode sit on the top and bottom boundaries respectively, with the voltage gradient vector acting downward. The voltage gradient and the vertical load increment together drive water flows between the elements and across the boundaries. The boundaries can be drained or undrained depending on the water accessibility. At time $t > 0$, the soil stratum is deformed as shown in Figure 1(b). It is assumed that the soil particles and water are incompressible, and only vertical deformation take place for the soil stratum. It is noteworthy that the model set-up is preferable to scenarios of sludge, tailings or hydraulic filling which usually start with a clear work space and allow laying the opposite electrodes in different levels. This set-up enables an electric field acting top-bottom, coinciding with the gravity force and surcharge preloading, and thus facilitating consolidation.

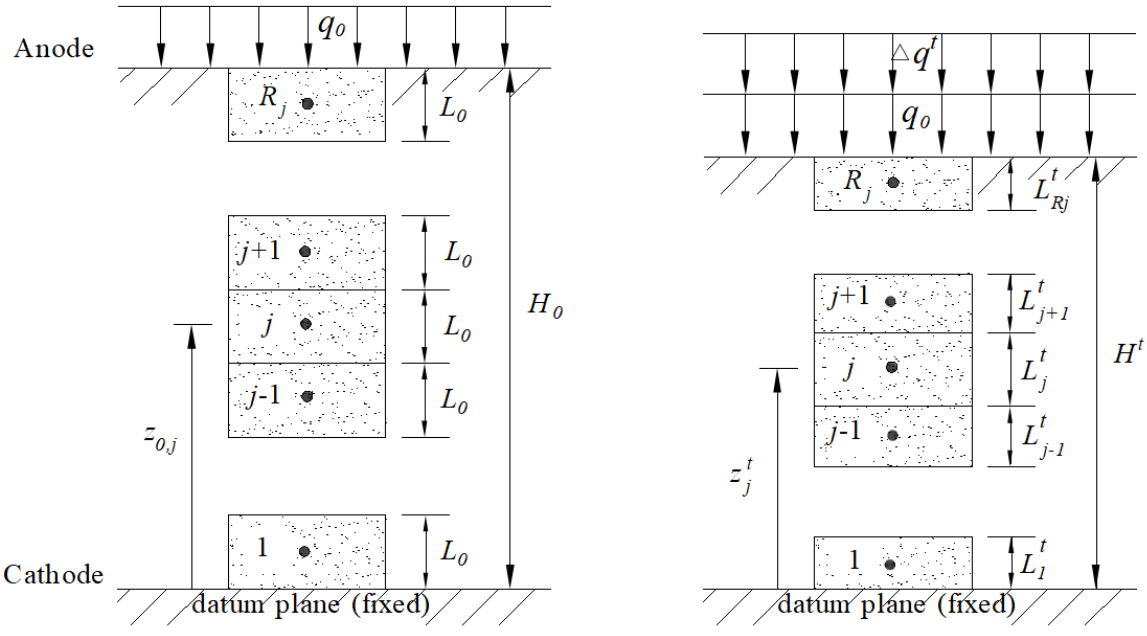

Figure 1 UEC2 model for a soil stratum subjected to the electro-osmosis–surcharge preloading consolidation: (a) before the consolidation ($t < 0$), (b) after the consolidation ($t \geq 0$).

115

116 ***2.2 Constitutive Relationships***

117 Model UEC2 adapts the methodology in model UEC1 in order to develop the
118 constitutive relationships. As shown in Figure 2, four constitutive relationship curves,
119 i.e., the compressibility, water conductivity, air permeability and soil–water
120 characteristic curve (SWCC), are plot. The compressibility curve [Figure 2 (a)] is
121 similar in development to those used in models of saturated soils, such as CS2 [17],
122 EC1 [18] and EC2 [19]. The curve is defined by R_m (≥2) pairs of the corresponding
123 void ratio $\hat{e}$ and the vertical effective stress $\hat{\sigma}'$, and is usually obtained from
124 oedometer tests. This compressibility curve however is used to examine components
125 of deformation related to saturation effects. The components arising from the
126 unsaturation effects are determined using the other three constitutive relationships.
127 From the relationships, the hydraulic conductivity, k_w, electro-osmotic conductivity, k_e,
128 air permeability, k_a, and the matrix suction, u_s, are a monotonic function of the degree
129 of saturation, S_r. Similarly, each of the relationships comprises ≥2 pairs of points: R_n
130 for the hydraulic conductivity, R_l the air permeability, R_k for the suction, which are
131 obtained from corresponding laboratory tests. Between the relationships, the degrees
132 of saturation use different notations in order to distinguish their values.

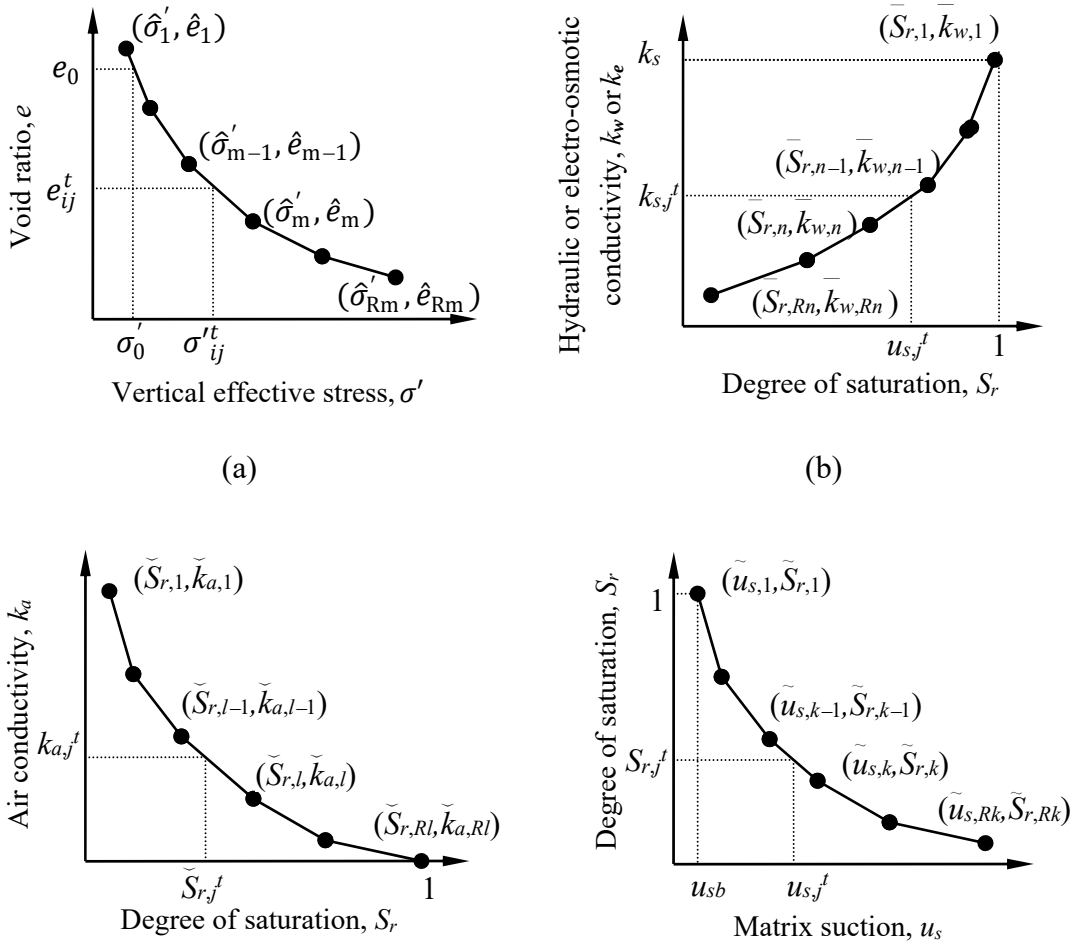

Figure 2 Constitutive relationships: (a) compressibility; (b) water permeability; (c) air permeability; and (d) soil–water characteristic curve.

The constitutive relationships can be modelled from mathematical approximations, as opposed to the laboratory tests. The compressibility curve [Figure 2(a)] of natural fine-grained soils is commonly represented by a semi-logarithmic relationship, which is expressed as

$$\Delta e / \Delta \log \sigma' = C_c \tag{1}$$

where C_c is compression index and determined experimentally. For Figure 2(b),

Mualem [20] predicted the hydraulic conductivity in terms of pore-size distribution. His predictions however are inaccurate for soils at near saturation stages [21]. To improve the accuracy, Tamagnini *et al.* [22] suggested to use the expressions as follow:

$$k_w = k_{wo} a_w S_r^{b_w} \tag{2}$$

$$k_a = k_d a_a \left(1 - S_r\right)^{b_a} \tag{3}$$

$$k_e = k_{eo} a_e S_r^{b_e} \tag{4}$$

where k_{wo} is hydraulic conductivity of saturated soil, k_d is air permeability of dry soil (i.e., at $S_r = 0$), k_{eo} is electro-osmotic conductivity of saturated soil; a_w, b_w, a_a, b_a, a_e and b_e are parameters and determined experimentally. An additional advantage of these expressions is the use of solo property S_r. One may argue the dependence on void ratio, which is reflected in the expressions by the permeabilities at the saturation state (e.g. k_{wo}). The SWCC relationship can be modelled in a range of forms as discussed in [23]. For general S-shaped retention curves (of fine-grained soils), van Genuchten [24] suggested to use the following expression

$$u_s = \frac{\left(S_e^{-\frac{1}{m_{vG}}} - 1\right)^{\frac{1}{n_{vG}}}}{\alpha_{vG}} \tag{5}$$

where S_e is the effective degree of saturation and expressed as $(S_r - S_{rs})/(1 - S_{rs})$, S_{rs} is the residual degree of saturation (i.e. the degree of saturation at which an increase in matric suction does not produce a significant change in S_r), α_{vG} is a parameter to scale the matric head, n_{vG} and m_{vG} are parameters determined experimentally, and obey the relationship $m_{vG} = (n_{vG} - 1)/n_{vG}$.

2.3 Stresses and Pore Pressures

Model UEC2 calculates the vertical total stress σ as the sum of the upper load and the self-weight of the compressible soil layer. When $t \geq 0$, the vertical total stress at node j is

$$\sigma_j^t = q_0 + \Delta q^t + \frac{L_j^t \gamma_j^t}{2} + \sum_{m=j+1}^{R_j} L_m^t \gamma_m^t \tag{6}$$

where j = 1, 2…. R_j. The values of j remain the same in the rest equations if not otherwise suggested. γ_j^t is the unit weight of element j and is equal to

$$\gamma_j^t = \frac{\left(G_s + S_{r,j}^t e_j^t\right)\gamma_w}{\left(1 + e_j^t\right)} \tag{7}$$

where G_s is the specific gravity of soil solids, γ_w is unit weight of water, $S_{r,j}^t$ is the degree of saturation of element j at time t, and e_j^t is its void ratio. The $S_{r,j}^t$ and e_j^t are determined in terms of the initial conditions and the developed consolidation algorithms. The effective stress at node j, $\sigma_j^{'t}$, can be calculated by interpolation from the compressibility curve [Figure 2(a)], as

$$\sigma_j^{'t} = \hat{\sigma}_{m-1}^{'} + \frac{\hat{e}_{m-1} - e_j^t}{a_{v,j}^t} \tag{8}$$

where the coefficient of compressibility, $a_{v,j}^t$, is the slope of the linear segment of the compressibility curve between the points ($\hat{\sigma}_{m-1}^{'}, \hat{e}_{m-1}$) and ($\hat{\sigma}_m^{'}, \hat{e}_m$) such that $\hat{e}_m \leq e_j^t \leq \hat{e}_{m-1}$.

Where the soil layer of interest is saturated at the outset, or remains saturated in the early stage of electro-osmosis, the pore water pressure at node j, $u_{w,j}^t$, is expressed as

$$u_{w,j}^t = \sigma_j^t - \sigma_j^{'t} \tag{9}$$

Along with the progress of electro-osmotic consolidation, the pore water pressure u_w decreases nonlinearly over the distance between the cathodes and anodes and, if the anodes are closed, becomes negative progressively from the anodes towards the cathodes [6, 12]. Provided that the matric suction, u_s, is expressed as

$$u_s = u_a - u_w \tag{10}$$

where u_a is the pore air pressure (relative to the atmosphere) and equal to zero if saturated, the matric suction emerges and increases with the negative pore water pressure u_w. When $u_s \geq u_{sb}$, where u_{sb} is the air-entry value of soil, air enters the soil pores of concern and the soils become unsaturated. Similar to the development of negative pore water, the unsaturated conditions evolve from the anodes to the cathodes to satisfy Eq. (10).

As per Bishop *et al.* [25], the pore air pressure, $u_{a,j}^t$, and the pore water pressure, $u_{w,j}^t$, at node *j*, if in its unsaturated condition, are respectively expressed as

$$u_{a,j}^t = \sigma_j^t - \sigma_j^{'t} + \chi_j^t u_{s,j}^t \tag{11}$$

$$u_{w,j}^t = u_{a,j}^t - u_{s,j}^t \tag{12}$$

where χ_j^t is the effective stress coefficient and as suggested by Aitchison [26] is estimated as

$$\chi_j^t = \frac{S_{r,j}^t}{0.4 S_{r,j}^t + 0.6} \tag{13}$$

The matric suction $u_{s,j}^t$ can be determined from the SWCC curve [Figure 2(d)] and expressed as

$$u_{s,j}^{t} = \tilde{u}_{s,k-1} + \frac{\tilde{S}_{r,k-1} - S_{r,j}^{t}}{b_j^t} \tag{14}$$

where b_j^t is the slope of the linear segment between the points $(\tilde{u}_{s,k-1}, \tilde{S}_{r,k-1})$ and $(\tilde{u}_{s,k}, \tilde{S}_{r,k})$ such that $\tilde{S}_{r,k} \le S_{r,j}^{t} \le \tilde{S}_{r,k-1}$. Eq. (11) provides equally reliable predictions of pore air pressures, as opposed to other solutions such as [27], and meanwhile offer simplicity by using the solo variant of S_r. This feature echoes the advantage discussed for the constitutive relationships.

2.4 Electrical Resistivity and Electric Potential

Electrical resistivity depends on soil properties, including the moisture content, mineralogy of solids, pore fluid, arrangement of voids, and degree of saturation [28]. Accounting for these factors, Komine [29] developed a model to determine the electrical resistivity of saturated porous media. Gong *et al.* [30] extended the model to unsaturated soils. Based on their models, the electrical resistivity of element j, ρ_j^t, is expressed as

$$\rho_j^t = \frac{1}{\frac{1}{\rho_s} \times \frac{1}{1+e_j^t} + \frac{1}{\rho_w} \times \frac{S_{r,j}^t e_j^t}{1+e_j^t}} \tag{15}$$

where ρ_s is the electrical resistivity of solids, and ρ_w is the electrical resistivity of pore fluid. In terms of Ohm's law, the electric potential at node j, V_j^t, is calculated as

$$V_j^t = \frac{\frac{\rho_j^t \times L_j^t}{2} + \sum_{i=1}^{j-1} \rho_i^t \times L_i^t}{\sum_{i=1}^{n} \rho_i^t \times L_i^t} \times V_m^t \tag{16}$$

213 ***2.5 Permeability, Flow Rate and Settlement***

214 The hydraulic conductivity, k_w, electro-osmotic conductivity, k_e, and the pore air
215 permeability, k_a, can be calculated from the water permeability relationship [Figure
216 2(b)], air permeability relationship [Figure 2(c)] and the corresponding degree of
217 saturation S_r. The equivalent hydraulic conductivity, $k_{ws,j}^t$, equivalent electro-osmotic
218 conductivity, $k_{es,j}^t$, and the equivalent air permeability, $k_{as,j}^t$, in series between the
219 nodes j and j+1 are calculated as

$$k_{xs,j}^t = \frac{k_{x,j+1}^t k_{x,j}^t \left(L_{j+1}^t + L_j^t\right)}{k_{x,j+1}^t L_j^t + k_{x,j}^t L_{j+1}^t} \tag{17}$$

220 where j = 1, 2…., R_j–1, and subscript 'x' represents 'w', 'e' and 'a', respectively.

221

222 The hydraulic flow rate, $q_{w,j}^t$, the electro-osmotic flow rate, $q_{e,j}^t$, and the air flow
223 rate, $q_{a,j}^t$, per unit flow area between nodes j and j+1 are calculated as

$$q_{x,j}^t = k_{xs,j}^t i_{x,j}^t \tag{18}$$

224 where j = 1, 2…., R_j–1, and $i_{x,j}^t$ is the gradient for pore water/air flow. The hydraulic
225 gradient, $i_{w,j}^t$, electro-osmotic gradient, $i_{e,j}^t$, and the pore air pressure gradient, $i_{a,j}^t$,
226 between nodes j and j+1 are respectively expressed as

$$i_{w,j}^t = \frac{h_{w,j+1}^t - h_{w,j}^t}{z_{j+1}^t - z_j^t} \tag{19}$$

$$i_{e,j}^t = \frac{V_{j+1}^t - V_j^t}{z_{j+1}^t - z_j^t} \tag{20}$$

$$i_{a,j}^t = \frac{h_{a,j+1}^t - h_{a,j}^t}{z_{j+1}^t - z_j^t} \tag{21}$$

227 where j = 1, 2…., R_j–1, the total hydraulic head, $h_{w,j}^t$, and the total pore air head,

228 $h_{a,j}^{t}$, at node *j*, are calculated as

$$h_{w,j}^{t} = z_{j}^{t} + \frac{u_{w,j}^{t}}{\gamma_{\mathrm{w}}} \tag{22}$$

$$h_{a,j}^{t} = \frac{u_{a,j}^{t}}{\gamma_{a}} \tag{23}$$

229 where γ_a is the unit weight of air and equals 12.65 N/m^3. The value is relatively
230 small and assumed constant in air compression.

231

232 The pore air is compressible, as opposed to the pore water or solids, if the pore air
233 pressures change. In terms of Boyle's law, the process of compression, arising from
234 the pore air flow, for element *j* in time step increment Δt, is expressed as

$$\left(u_{a,j}^{t+\Delta t} + p_a\right) A_{a,j}^{t+\Delta t} = \left(u_{a,j}^{t} + p_a\right) A_{a,j}^{t} - \left(q_{a,j}^{t} - q_{a,j-1}^{t}\right)\Delta t \tag{24}$$

235 where $u_{a,j}^{t+\Delta t}$ and $A_{a,j}^{t+\Delta t}$ are the pore air pressure of element *j* and the volume of
236 pore air of element *j* (per unit flow area), after the combination of air compression and
237 air flow, $u_{a,j}^{t}$ and $A_{a,j}^{t}$ are the corresponding values before the compression/air
238 flow process, and p_a is one atmosphere and equals 101.3 kPa, and is included as the
239 base pressure. Rearranging Eq. (26), the volume of pore air is obtained as

$$A_{a,j}^{t+\Delta t} = \frac{\left(u_{a,j}^{t} + p_a\right) A_{a,j}^{t} - \left(q_{a,j}^{t} - q_{a,j-1}^{t}\right)\Delta t}{u_{a,j}^{t+\Delta t} + p_a} \tag{25}$$

240 For element *j*, the height, $L_j^{t+\Delta t}$, void ratio, $e_j^{t+\Delta t}$, and the degree of saturation, $S_{r,j}^{t}$,
241 are updated to

$$L_j^{t+\Delta t} = L_j^{t} - \left(q_{w,j}^{t} - q_{w,j-1}^{t} + q_{e,j-1}^{t} - q_{e,j}^{t}\right)\Delta t - \left(A_{a,j}^{t} - A_{a,j}^{t+\Delta t}\right) \tag{26}$$

$$e_j^{t+\Delta t} = \frac{L_j^{t+\Delta t}\left(1 + e_{0,j}\right)}{L_{0,j}} - 1 \tag{27}$$

$$S_{r,j}^{t+\Delta t} = 1 - \frac{A_{a,j}^{t+\Delta t}\left(1+e_j^{t+\Delta t}\right)}{L_j^{t+\Delta t} e_j^{t+\Delta t}} \tag{28}$$

242 At time step t, the height, H^t, surface settlement, S^t, and the degree of
243 consolidation, U^t, of the soil layer are calculated as

$$H^t = \sum_{j=1}^{n} L_j^t \tag{29}$$

$$S^t = H_0 - H^t \tag{30}$$

$$U^t = \frac{S^t}{S_f} \tag{31}$$

244 where S_f is the final settlement of the soil layer when all streams of fluid/air flows
245 reach equilibrium or consolidation is completed. As applied in [18, 19], the criterion
246 of equilibrium is to set a significantly small value versus the increment of surface
247 settlement.

248

249 ***2.6 Load-Induced Pore Air Compression and Settlement***

250 In unsaturated conditions, the volume of pore air is compressible when the load
251 increment, Δq^t, in Figure 1 is applied. The air compression re-allocates stresses borne
252 respectively by the soil solids, pore water and pore air, and the individual stresses are
253 determined by an iterative approach extended from Yin and Ling [31]. We defined a
254 small incremental void ratio, Δe, (i.e., –0.001), and for element j added a multiple of
255 the increment to the initial void ratio e_j^t, which is expressed as

$$e_j^i = e_j^t + i\left(\Delta e\right) \tag{32}$$

256 where step i = 1, 2, 3, …. At the ith step, the vertical total stress, σ_j^i, as per Eqs.
257 (11)–(12), can be written as

$$\sigma_j^i = \sigma_j'^i + \left(1-\chi_j^i\right)u_{a,j}^i + \chi_j^i u_{w,j}^i \tag{33}$$

As presented in Eq. (8), the effective stress of node *j* at step *i*, $\sigma_j'^i$, can be determined in terms of the compressibility curve [Figure 2(a)] and the corresponding void ratio e_j^i. The pore air pressure, $u_{a,j}^i$, pore water pressure, $u_{w,j}^i$, and the effective stress coefficient, χ_j^i, are then determined considering the pore air compression. We defined the pore air ratio, e_a, as the volume of air to the volume of solids. In terms of Boyle's law, the compression of pore air in element *j*, obeys the following expression:

$$\left(u_{a,j}^t + p_a\right)e_{a,j}^t = \left(u_{a,j}^i + p_a\right)e_{a,j}^i \tag{34}$$

where $u_{a,j}^t$ and $e_{a,j}^t$ are the pore air pressure and pore air ratio before the compression, $u_{a,j}^i$ and $e_{a,j}^i$ are corresponding values after the *i*th incremental step. From the phase relationship, the pore air ratio e_a can be written as

$$e_a = e\left(1-S_r\right) \tag{35}$$

Substituting Eq. (35) into Eq. (34), we have

$$\left(u_{a,j}^t + p_a\right)e_j^t\left(1-S_{r,j}^t\right) = \left(u_{a,j}^i + p_a\right)e_j^i\left(1-S_{r,j}^i\right) \tag{36}$$

where e_j^i and $S_{r,j}^i$ are the void ratio and the degree of saturation of element *j* at step *i*. As the compression is instantaneous, the moisture content of element *j* remains unchanged before and after. This law of conservation of mass yields the following equation:

$$\frac{S_{r,j}^t e_j^t}{G_s} = \frac{S_{r,j}^i e_j^i}{G_s} \tag{37}$$

Combining Eqs. (36) and (37), the pore air pressure of node *j* at step *i*, $u_{a,j}^i$, is obtained as

$$u_{a,j}^{i}=\frac{\left(u_{a,j}^{t}+p_a\right)e_j^t\left(1-S_{r,j}^{t}\right)}{e_j^i-S_{r,j}^{t}e_j^t}-p_a \tag{38}$$

274 The pore water pressure of node *j*, $u_{w,j}^{i}$, equals

$$u_{w,j}^{i}=u_{a,j}^{i}-u_{s,j}^{i} \tag{39}$$

275 where $u_{s,j}^{i}$ is the matric suction of node *j* at step *i*. As presented in Eq. (14), the
276 suction can be determined from the SWCC curve [Figure 2(d)] and the corresponding
277 degree of saturation $S_{r,j}^{i}$. The $S_{r,j}^{i}$ can be determined in terms of Eq. (37), and is
278 used to calculate the effective stress coefficient χ_j^i as presented in Eq. (13).
279 Substituting $\sigma_j'^i$, $u_{a,j}^{i}$, $u_{w,j}^{i}$ and χ_j^i into Eq. (33), we can obtain the total vertical
280 stress σ_j^i. If σ_j^i is equal to σ_j^t, the vertical total stress as specified in Eq. (6), or the
281 difference between them is less than a pre-set small value, the form is closed and the
282 iterations (for the pore air compression) terminate at step *i*. Otherwise, the loop
283 continues to step *i*+1.

284

285 Following the pore air compression, the element height, L_j^i, layer height, H^i, and
286 the surface settlement, S^i, are updated as

$$L_j^i=\frac{\left(1+e_j^i\right)L_{0,j}}{\left(1+e_{0,j}\right)} \tag{40}$$

$$H^i=\sum_{j=1}^{R_j}L_j^i \tag{41}$$

$$S^i=H_0-H^i \tag{42}$$

287 It is noteworthy that model UEC2 is able to account for the load-induced pore air
288 compression that occurs anytime in the middle of consolidation, as opposed to at the
289 outset of t = 0. The algorithms of pore air compression will read off the current

290 consolidation results (e.g., vertical stresses, void ratio, pore water/air pressures)
291 obtained from the algorithms of consolidation, and update the results for consolidation
292 analysis.

293

294 ***2.7 Boundary Conditions and Time Step Increment***

295 Model UEC2 uses the boundary conditions as provided in Table 1.

296 Table 1 Model UEC2 boundary conditions

Locations	Open (free access to water and air)	Closed (no access to water and air)
Cathode	$i_{e,0}^t = V_1^t / z_1^t$, $i_{w,0}^t = \left(h_1^t - h_{wb}\right) / z_1^t$, and $i_{a,0}^t = h_{a,1}^t / z_1^t$	$i_{e,0}^t = 0$, $i_{w,0}^t = 0$, and $i_{a,0}^t = 0$
Anode	$i_{\mathrm{e},R_j}^t = \left(V_{\mathrm{m}}^t - V_{R_j}^t\right) / \left(H^t - z_{R_j}^t\right)$, $i_{w,R_j}^t = \left(h_{wt} - h_{R_j}^t\right) / \left(H^t - z_{R_j}^t\right)$, and $i_{a,R_j}^t = -h_{a,R_j}^t / \left(H^t - z_{R_j}^t\right)$	$i_{e,R_j}^t = 0$, $i_{w,R_j}^t = 0$, and $i_{a,R_j}^t = 0$

297 Note: h_{wt} is the total hydraulic head at the top boundary; h_{wb} is the total hydraulic
298 head at the lower boundary.

299

300 Model UEC2 adapts the criteria for time step increment that were used in models CS2
301 [17] and EC1 [18]. For the defined model geometry, the criteria are updated as

$$\Delta t = \min\left\{\frac{\alpha a_{v,j}^t \left(L_j^t\right)^2}{k_{w,j}^t \left(1+e_j^t\right)}, \left|\frac{0.01 L_0 \left(e_{0,j} - e_{f,j}\right)}{\left(1+e_{0,j}\right)\left(q_{w,j}^t - q_{w,j-1}^t + q_{e,j-1}^t - q_{e,j}^t + q_{a,j-1}^t - q_{a,j}^t\right)}\right|\right\} \quad (43)$$

302 where coefficient $\alpha \approx 0.4$ as per [17], and $e_{f,j}$ is the final void ratio of element j and is

303 determined in terms of the iterations suggested in [19]. In Eq. (43), the first criterion
304 is to govern the frequency of the calculation in response to the vertical flow, which is
305 a step to align the numerical results with the solutions for Terzaghi's 1D consolidation
306 theory; the second is to ensure no more than 1% of final settlement of the element
307 developed in a time step increment.
308
309 **3. Computer Program**
310 A flow diagram illustrating the algorithms of the computer program is presented in
311 Figure 3. The input properties include the number of elements (R_j), initial height of
312 soil layer (H_0), specific gravity of solids (G_s), electrical resistivity of pore fluid (ρ_w)
313 and solids (ρ_s), effective voltage (V_m^t), applied stresses (q_0, Δq^t), constitutive
314 relationships, boundary conditions, and the termination criteria for the program. After
315 UEC2 reads the input data, the initial height (L_0), the initial elevation ($z_{0,j}$) and the
316 initial void ratio ($e_{0,j}$) of element j are calculated. When the effective voltage (V_m^t)
317 and vertical load increment (Δq^t) are applied, the loop starts, and each element
318 updates its properties over the time increment (Δt). Between the loops, if element j
319 becomes unsaturated and additional load increment is applied, i.e., $\Delta q^t > \Delta q^{t-\Delta t}$, the
320 volumes of pore air in the element compress, triggering the sub-loop on the left-hand
321 side. In the stage of compression, the element properties ($\sigma_j'^i$ $S_{r,j}^i$ $u_{s,j}^i$ $u_{a,j}^i$ $u_{w,j}^i$) are
322 updated with the multiple of void ratio increment (Δe), until $\sigma_j^j = \sigma_j^t + \Delta q^t$. The
323 updated element properties (e_j^i $S_{r,j}^i$ L_j^i) and the layer geometry (H^i S^i) feed to the
324 main loop. The calculations terminate when consolidation time $t \geq t_f$, or settlement

in an time increment $\Delta S \le m$, where t_f and m are a user-specified elapsed time and a sufficiently small settlement value, respectively. When $\Delta S \le m$, it is suggested that the consolidation has reached equilibrium of seepage and has ended. Then the final surface settlement (S) and the average degree of consolidation (U^t) are calculated. The flow diagram was programmed using FORTRAN software package.

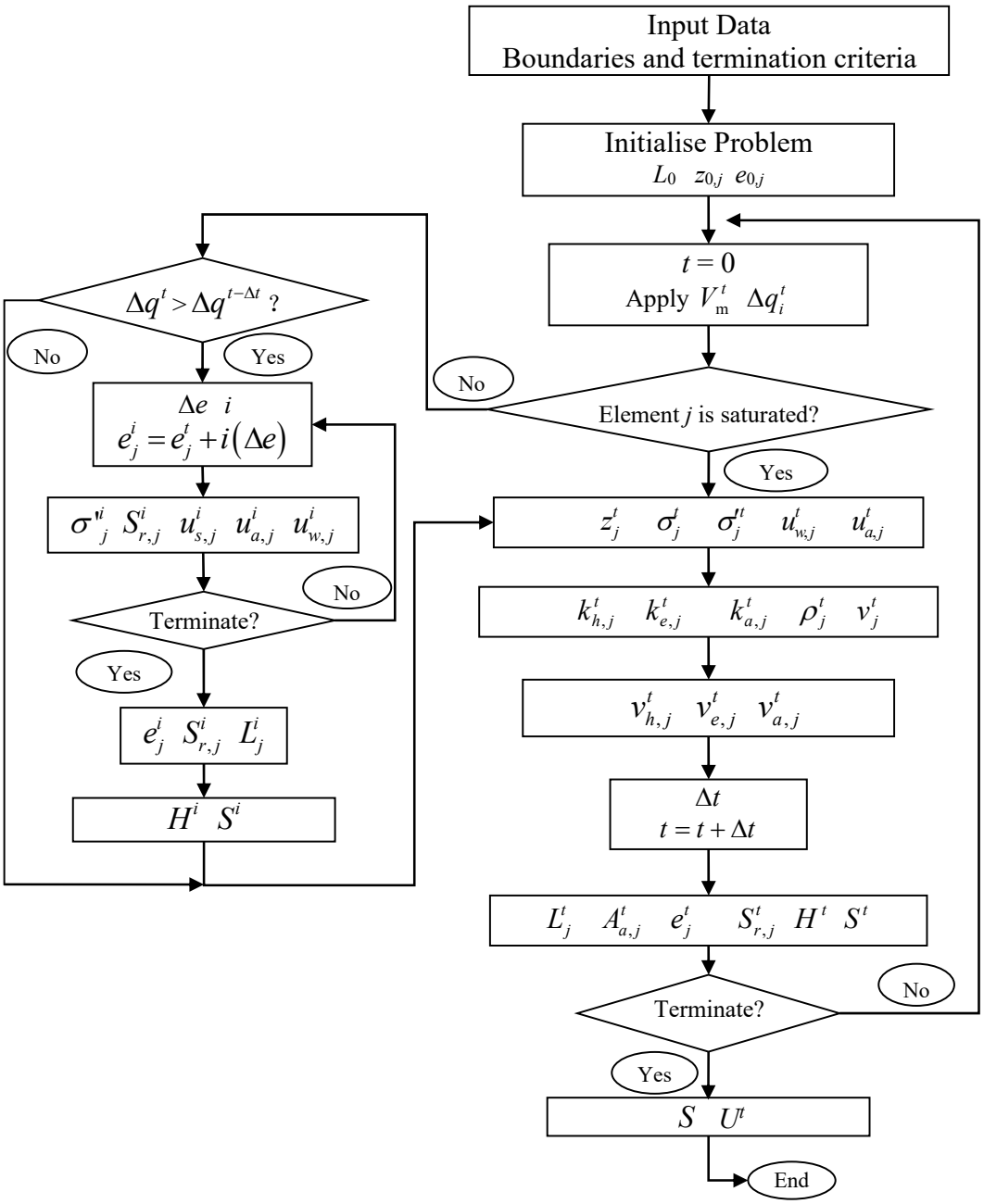

Figure 3 Flow chart of model UEC2

4. Model Validation

4.1 Material and Model Parameters

The material used in the model validation test was a remoulded clay soil. The soil was recovered from the Lingang Industrial Zone of Tianjin, China. The physical properties of the soil are provided in Table 2. The Atterberg limits lie just below the A-line, and the soil is classified as MH, clayey silt of high plasticity, in terms the Unified Soil Classification System. The SWCC curve was obtained by using the GCTS Fredlund SWCC device at a capacity of 0–1,500 kPa. A set of ten soil specimens of varied water contents were subjected to the suction tests. The test results are presented in Figure 4. The results were then modelled against the ven Genuchten model [Eq. (5)], in terms of the fitting function provided in Matlab software package. The modelling yielded parameters α, n, and S_{rs} as 0.022 kPa^{-1}, 1.293 and 0.24, respectively, with a coefficient of relevance R^2 = 99.2%. The hydraulic conductivity was measured using the falling-head method. The value is k_{wo} = 7.6×10^{-9} m/s which classifies the specimen a less-permeable soil. For clayey silt, the air permeability does not vary significantly and usually falls onto the order of magnitude of 1×10^{-7} m/s which was presumed in the current study. The electro-osmotic conductivity at saturation was obtained using the permeameter developed in [1]. This device enables greater accuracy by avoiding the influence arising from hydraulic flow. The result was 4.5×10^{-9} m^2/s·V. The electrical resistivities of pore fluid and solids were determined using the Miller's box as suggested in [1]. The results were 6 Ω·m for the pore fluid

354 and 1,000 Ω·m for the solids. The values largely agree with the results obtained in [1].
355 It involves complicated and tedious processes to calibrate the parameters required for
356 the constitutive relationships as specified in Eqs. (2)–(4). The parameters however are
357 constant and independent on soil types [20]. For these forms, Tamagnini *et al.* [22]
358 suggested to use the parameters of b_e=3.2, a_w=a_a=1, and b_w= b_a =5.

359 Table 2 Physical properties, permeability and electrical resistivity of the soil sample

Property	Value
Plastic limit, w_P (%)	31
Liquid limit, w_L (%)	52
Specific gravity of solids, G_s	2.7
Water content, w_0 (%)	92.6
Initial void ratio, e_0	2.53
Compression index, C_c	0.62
Residual degree of saturation, S_{rs}	0.24
Parameter in Eq. (5), α_{vG} (kPa^{-1})	0.022
Parameter in Eq. (5), n_{vG}	1.293
Hydraulic conductivity of saturated soil, k_{wo} (m/s)	7.6×10^{-9}
Exponent for hydraulic conductivity [Eq. (2)], b_w	5
Air permeability of dry soil, k_d (m/s)	1×10^{-7}
Parameter for air permeability [Eq. (3)], b_a	5
Electro-osmotic conductivity of saturated soil, k_{eo} (m^2/s·V)	4.5×10^{-9}
Parameter for electro-osmotic conductivity [Eq. (4)], b_e	3.2

Parameters for permeability, $a_w = a_a = a_e$	1
Electrical resistivity of pore fluid, ρ_w (Ω·m)	6
Electrical resistivity of the solids, ρ_s (Ω·m)	1,000

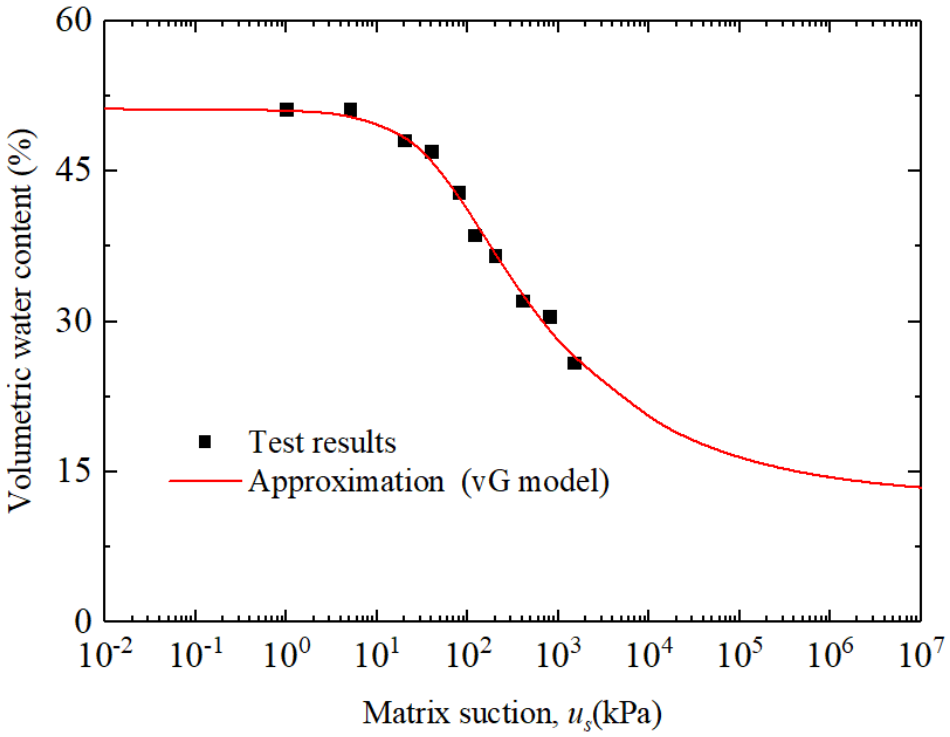

Figure 4 Soil SWCC curves obtained from tests and simulations.

4.2 Experimental Set-up

The experimental set-up is presented Figure 5. The set-up includes a consolidation cylinder of ∅200 (*I.D.*) × 600 (*H*) mm and 10 mm wall thickness. The cylinder is made of transparent, rigid polycarbonate material, enabling observations of consolidation results. The cylinder is closed at the bottom and open at the top. The bottommost is a 50 mm thick sand filter and a drain perforated on the wall. The volume of water passed through the drain is collected as an underflow and measured using a graduated cylinder. Above the sand cushion is the cathode which is a stainless

371 steel disc of ∅200 × 1 (*H*) mm. The disc surface is perforated with a total of 48 holes
372 of ∅6 mm, enabling water drainage. On the cylinder wall a small water-proof hole is
373 perforated at the same height as the disc, and used to wire the cathode to the DC
374 power source. Above the disc is one layer of cotton fabric used to prevent passages of
375 fine particles. On the fabric, a soil column of 500 mm high is filled up. The soils were
376 prepared in a mixer, at a moisture content of 92.6% (100% intended). This moisture
377 content allows the soils to sit in the liquid state, thus enabling a nearly saturated
378 condition. The soils were transferred into the consolidation cylinder in layers, 100 mm
379 height each. Each lift was poured under free gravity, with an agitator slightly mixing
380 the soils. The liquid state itself facilitated the self-compaction and largely even
381 distribution of the soils as presented in Figure 5b. As the soils were fine-grained, the
382 soils exhibited high viscosity and there was no noticeable segregation when the soils
383 were placed. Similarly, on the upper end of the soil column sits the layers of cotton
384 fabric, anode and loading pad, forming the upper boundary of the consolidation
385 system. The anode is a stainless steel mesh of 10 × 10 mm apertures. The loading pad
386 includes a polycarbonate disc of ∅200 × 10 (*H*), perforated with a grid of ∅1 mm
387 openings, and a pad of ∅100 mm. The pad and the polycarbonate disc together enable
388 a uniform pressure acting downward. The dead load was applied through the leverage
389 system of oedometer unit. A dial gauge was mounted on the upper boundary to record
390 the surface settlement.

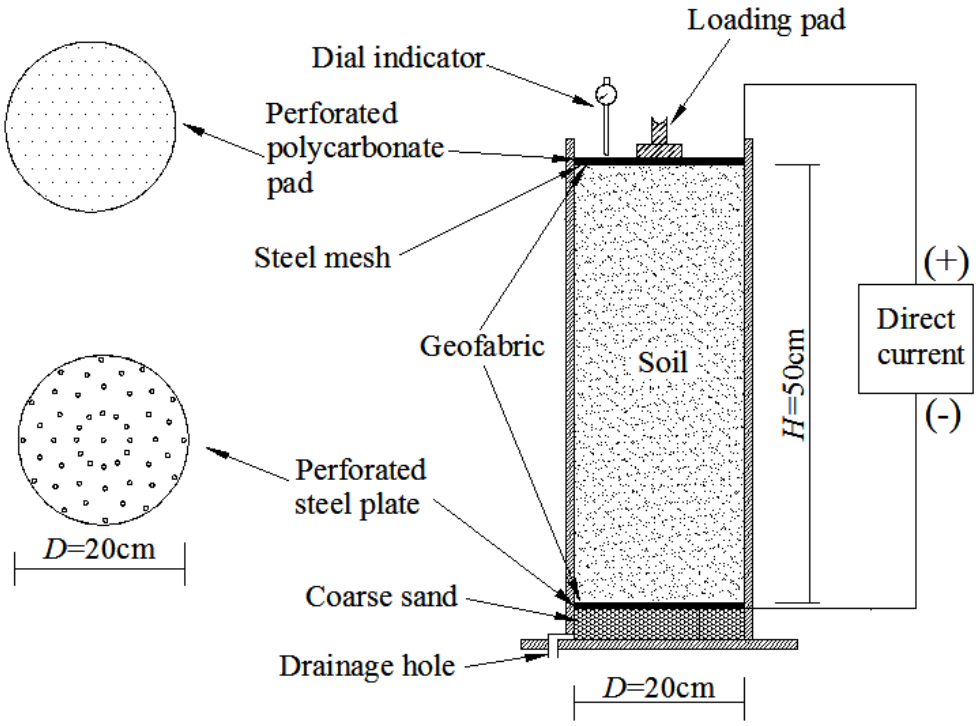
Loading pad
Dial indicator
Perforated
polycarbonate
pad
Steel mesh
Geofabric
Soil
H=50cm
(+)
Direct
current
(-)
Perforated
steel plate
D=20cm
Coarse sand
Drainage hole
D=20cm

(a)

(b)

(c)

Figure 5 The experimental set-up for electro-osmosis–surcharge preloading combined consolidation: (a) the set-up diagram, (b) the plan view of soil sample in the cylinder before consolidation, and (c) the soil sample in the cylinder subjected to the consolidation.

We designed two test scenarios: tests 1 and 2, as presented in Table 3. Both tests used the same voltage V_m =30 V and surcharge preloading Δq = 50 kPa. The two tests however applied the surcharge load in different means: one-step loading for test 1 and stepped loading for test 2. In test 2, the total load were 12.5, 25 and 50 kPa applied at t = 0, 27.3 and 48 hours respectively. The stepped loading scenario was to examine possible consolidation efficiency arising from the multiple steps of loading, to cross-check the performance of the model, more importantly, to assess the influence of load increments on unsaturated soils. It is noteworthy that V_m =30 V was used as

410 the effective voltage transmitted through the body of soil. The voltage losses at the
411 electrodes due to gap effects and chemical reactions were negligible as the surcharge
412 preloading was able to minimise (if not avoid) it by acting downward. This voltage
413 applies a voltage gradient of i_e = 60 V/m to the soil column which agrees with the
414 ranges used in earlier studies.

415 Table 3 Test scenarios for electro-osmosis–surcharge preloading consolidation.

Test	Voltage V_m	Load Δq
1	30 V applied at t = 0 hour	50 kPa applied at t = 0 hour
2	30 V applied at t = 0 hour	12.5, 25, 50 kPa applied at 0, 27.3 and 48 hours, respectively

416

417 ***4.3 Results and Discussion***

418 The results of tests 1 and 2 are presented in Figure 6. The results include the surface
419 settlement and the volume of water discharged over elapsed time. It lasted 129.3 h for
420 test 1 and 97 h for test 2, when the settlement curves became flat out eventually. The
421 recorded final settlement was 91.4 mm in test 1 and 84.0 mm in test 2, corresponding
422 to settlement rates of 18.3% and 16.8% respectively. Both settlement rates are
423 significant and thus enable large-strain consolidation scenarios. The volumes of water
424 discharge keep increasing over time and are 3,950 mL in test 1 and 3,500 mL in test 2.
425 From the test results, test 1 of one-step loading outperforms test 2 of stepped loading
426 in regard to the settlement and water discharge, provided the same elapsed time is
427 considered. It is noteworthy that the component of surcharge loading contributes to a
428 major proportion of settlement, whereas the electro-osmosis component accelerates
429 the settlement and reduces the elapsed time. The trades-off between the settlement and

time have been discussed in earlier studies [1, 8].

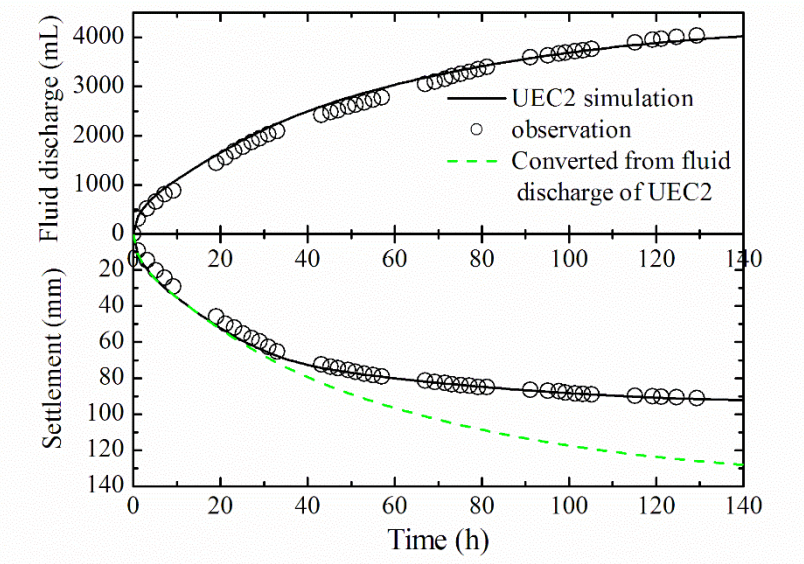

(a)

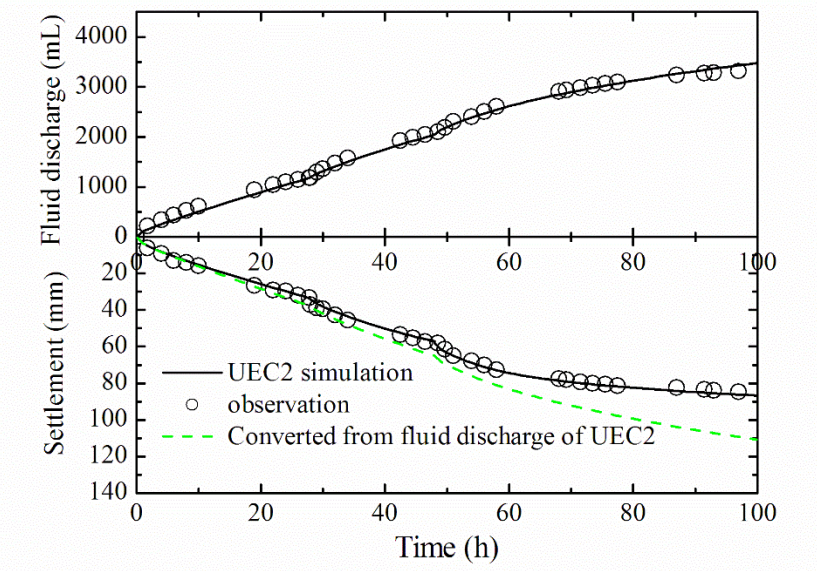

(b)

Figure 6 Soil settlement and water discharge versus elapsed time for: (a) test 1 of one-step loading, and (b) test 2 of stepped loading.

Model UEC2 was applied to simulate the consolidation of the two tests. The model meshed the soil column into R_j = 50 elements, from the bottom to the top. Each

element was 10 mm high, which as per [18], was thin enough to allow a small-strain condition. Each of the elements was assigned the properties provided in Table 2. At the anode, the boundary condition is open for hydraulic flow if $u_{w,R_j}^t \geq 0$, otherwise closed, and is open for air flow. At the cathode, the boundary is open for water and air. The modelling results of the two tests are provided in Figure 6. Excellent agreement between the test and simulation results is obtained for both tests. The model is even capable of capturing the instantaneous drops of settlement arising from the stepped loading. We also calculated the surface settlement of soil column in terms of the simulated volumes of water discharge, presuming a saturated condition throughout. The settlement results exceed the corresponding results obtained in the tests and simulations. The differences by itself represent the volumes of air entry. The volumes of air grow over time.

In addition to the settlement, measurements including pore water pressure and suction pressure can further examine performance of consolidation. These measurements however were less viable as far as the soil column was examined, due to accessibility and QA/QC issues. Alternatively, we managed to measure soil water contents, an equally important indicator of dewatering results, across the depth of soil column. We recovered a total of four soil specimens at the end of each test. The locations were z = 50, 152, 260, 370 mm approximately. The water content results of the two tests, together with the simulation results of different elapsed times, are presented in Figure 7. Similarly excellent agreement between the test and simulation results is obtained

462 for both tests. This agreement, together with the agreement in settlement and water
463 discharge predictions, suggests that model UEC2 is validated to simulate the
464 electro-osmosis–surcharge preloading combined consolidation of unsaturated soils. It
465 is noteworthy that the water contents increase largely linearly with the elevation at the
466 end of each test, and prior to the ends are varied nonlinearly. It is also noted of the
467 water contents at the cathodes: a constant value of 75% in test 1 and varied values 84%
468 to 75% in test 2. The difference arises from the stepped loading mode versus the
469 one-step loading mode. The one-step loading is able to squeeze greater volume of
470 water than the stepped loading does where the other conditions remain the same.

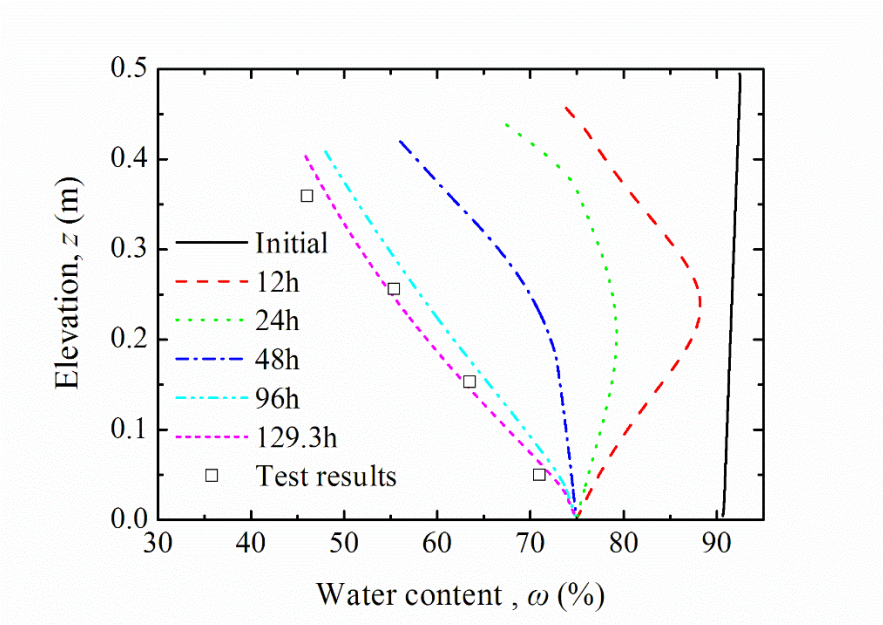

471

472 (a)

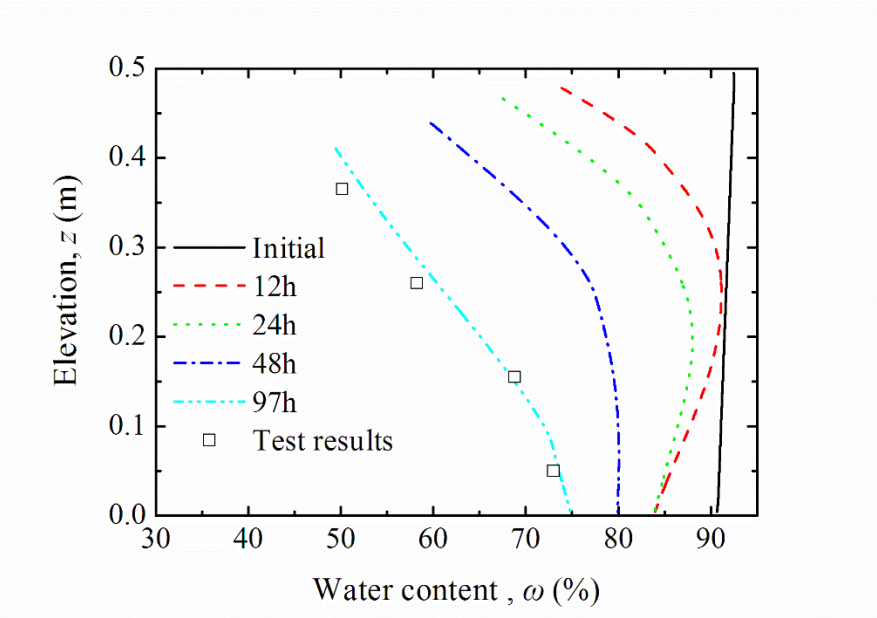

(b)

Figure 7 Water content profiles versus elapsed time for: (a) test 1 of one-step loading, and (b) test 2 of stepped loading.

5. Simulation Results

To gain an insight into the performance of electro-osmosis–surcharge preloading combined method, the isochrones of pore water pressure, pore air pressure and the degree of saturation, obtained for test 1 (i.e., the one-step loading scenario), are obtained from model simulations, and provided in Figure 8. The time points for the isochrones include t = 12, 24, 48, 96 and 144 h. Over the elapsed time, the pore water pressures across the depth decrease from 50 kPa (i.e., the applied level of surcharge loading) at the outset, to zero at time between 24 h to 48 h, and subsequently become negative throughout. Nonlinear changes of pressure occur over time. Similar nonlinearity occurs to the pressure changes across depth. At any of the examined time points, the corresponding isochrone is curvy, with the pore pressures at bottom

cathode remaining zero (due to the open access to free water) and the pressures at the rest locations varied by depth. The closer the locations are near the anode, the greater change (to negative pressure) it will be. The greatest negative pressure of –220 kPa occurs to the location z = 0.4 m at t = 144 h. As suggested in [18], this level of force would have caused soil cracks if the vertical loading were not applied. Above this depth, i.e., z = 0.4 to 0.5 m, the pore water pressures do not exist. Same results occur to the similar locations at earlier time points. The non-existence of pore pressure suggests the emergence of completely dry condition in proximity to the anode, which ends up increasing the electrical resistivity, and a loss of power energy.

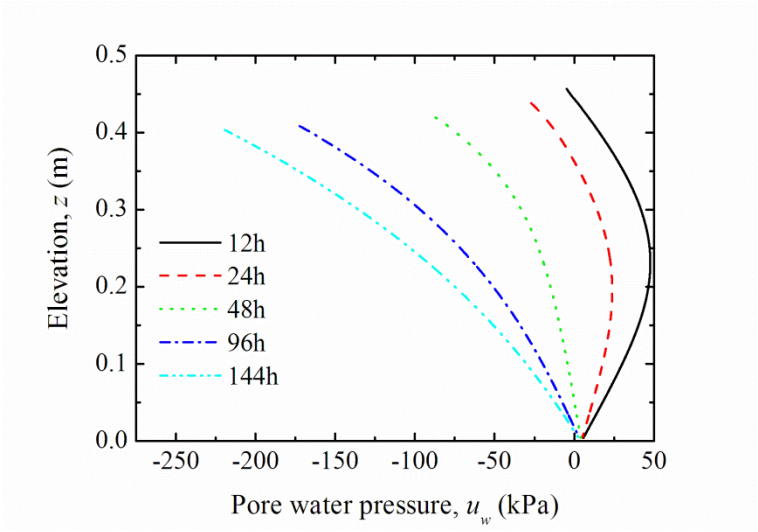

(a)

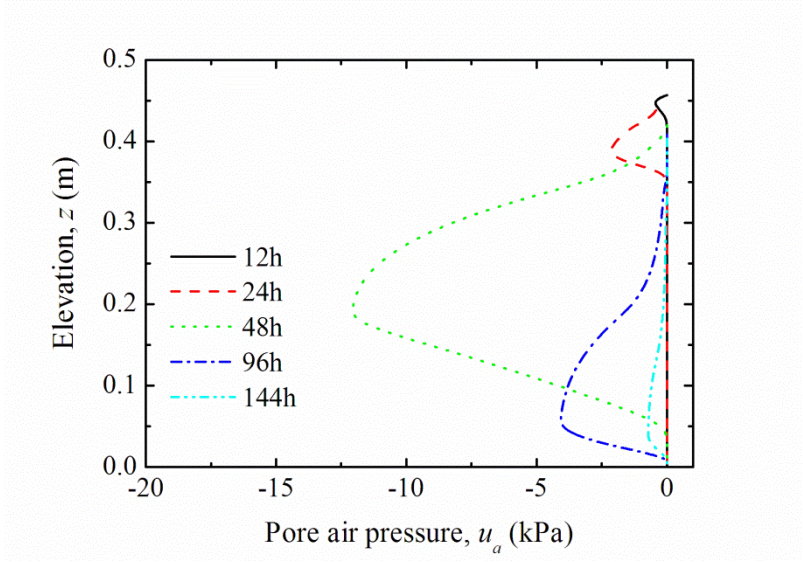

(b)

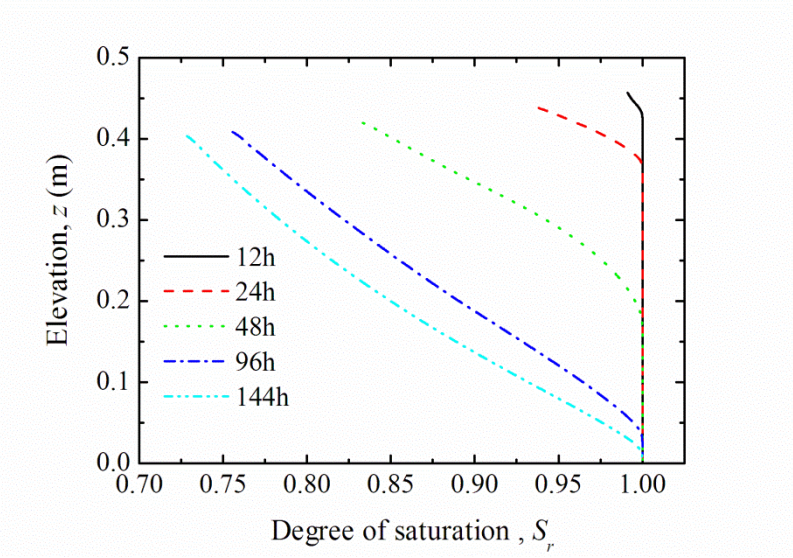

(c)

Figure 8 Isochrones of (a) pore water pressure, (b) pore air pressure, and (c) the degree of saturation, of soil column in test 1 of one-step loading.

The isochrones suggests the presence of two stages: dissipation of positive pore pressure and evolvement of negative pore pressure. For test 1, the transition point was approximately at t = 40 hours. In the first stage, electro-osmosis works mainly

towards accelerating the pore pressure dissipation. In the second stage, the soils become unsaturated, progressively on time and locations. When unsaturated conditions occur, maintaining electro-osmosis processes adds to removal of additional volume of water and sort of further settlement, as presented in Figure 6. An additional benefit lies in strength gain and densification of the unsaturated soils via compaction if deployed in the field.

As opposed to the curvy isochrones of pore water pressures, the corresponding isochrones of pore air pressures are varied significantly, in both time- and space domains, as presented in Figure 8b. It appears that each isochrone is represented by a solo waveform, with varied amplitudes between the recorded time points. The amplitude is a small value of –0.5 kPa presented at location z = 0.45 m at t = 12 h. With time elapsing, the amplitudes increase to the greatest value of –12 kPa t = 48 h and then decrease; the corresponding locations travel down towards the cathode. At t = 144 h, the amplitude decreases to –0.7 kPa and the corresponding location relocates to z = 0.35 m. Similar to the amplitude, the breadth of the waveform increases and then decreases. The air enters the soil regime due to the evolvement of unsaturated conditions, and the development of pore air pressure is dependent on multiple factors, e.g. the pore water pressure, accessibility to atmosphere and soil permeability. At the outset, the negative pore water pressure, as per [6], emerges but is small, and its presence is restricted to the locations near the anode. The emerged pore water pressure needs to be balanced in terms of Eqs. (11)–(12), and if the resulting pore air

pressure exceeds the soil air-entry value, a volume of air enter, developing the pore air pressure, as of the isochrone obtained at t = 12 h. Over time, the locations of influence expand from the anode to the cathode and the air-entry processes continue if the top boundary remains open. The continuous inflow of air, if adequate in volume, is able to minimise the deficiency of air, thus offsetting the resulting pore air pressure. The efficiency of pressure reduction is distance-dependent. The farther from the entry point of the anode, the less noticeable the pressure reduction, if the pore water pressure keeps increasing. The fact is that the pore water pressures reach equilibrium, whereas the voltage gradient remains unchanged [6]. The continuous inflow of air is able to occupy, progressively downward, the pore space and reduce the pore air pressure, which explains the gradual flat-outs of pore air pressure isochrones.

As expected, the degrees of saturation are time-and distance dependent, as presented in Figure 8c. Over the examined time points, the soil column becomes unsaturated, progressing from the anode to the cathode. The closer to the anode, the greater elapsed time, the more noticeable the unsaturated condition will be. At location z = 0.4 m and time t = 144 h, the least degree of saturation is present, with the degree of saturation of S_r = 0.73. Above this location, S_r = 0, suggesting a dry condition, which echoes the non-existence of pore water pressure presented in Figure 8a. It is noteworthy of the linearity of the degree of saturation as opposed to the depth over the unsaturated sections. The linear relationships agree with the water content profiles obtained in the tests (Figure 7).

To examine responses of soil to the stepped loading, in particular, the air compression under unsaturated conditions, we looked into individual elements of soil column subjected to test 2 (i.e., the stepped-loading scenario) and extracted their consolidation results, as presented in Figure 9. The results provide the pore water pressure, pore air pressure and the degree of saturation over the elapsed time for three elements: j = 5, 25 and 46. The three elements sit on or near to the cathode, the mid-height and the anode respectively.

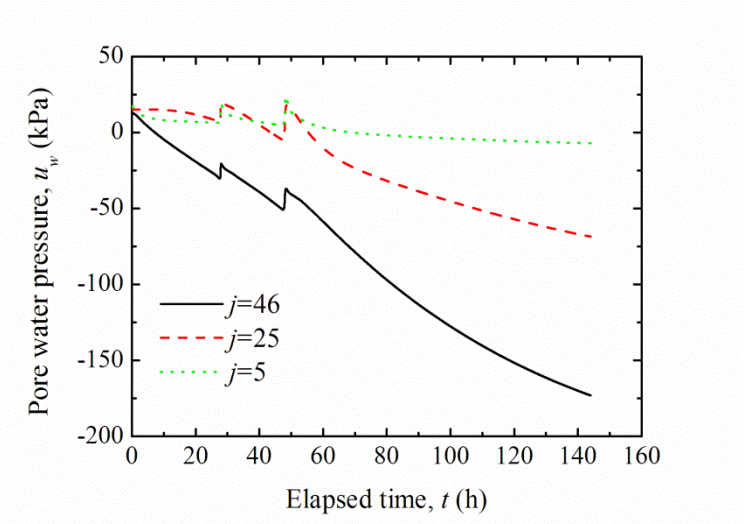

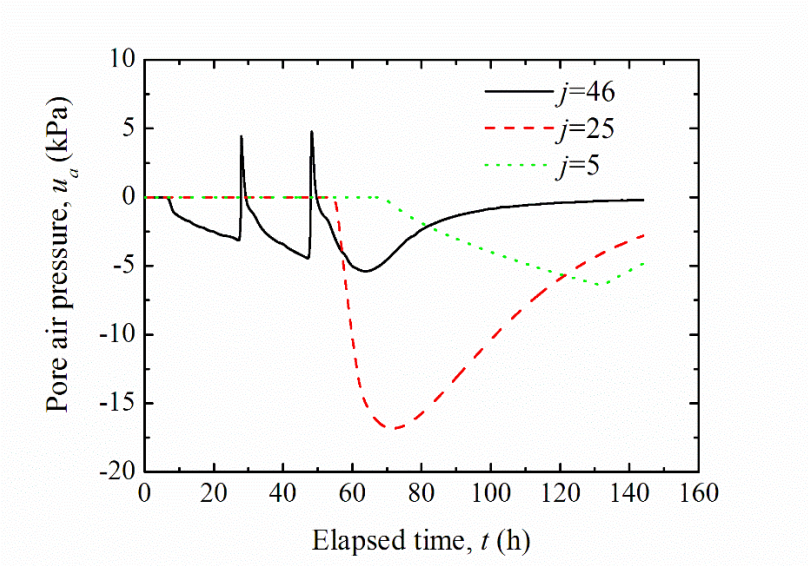

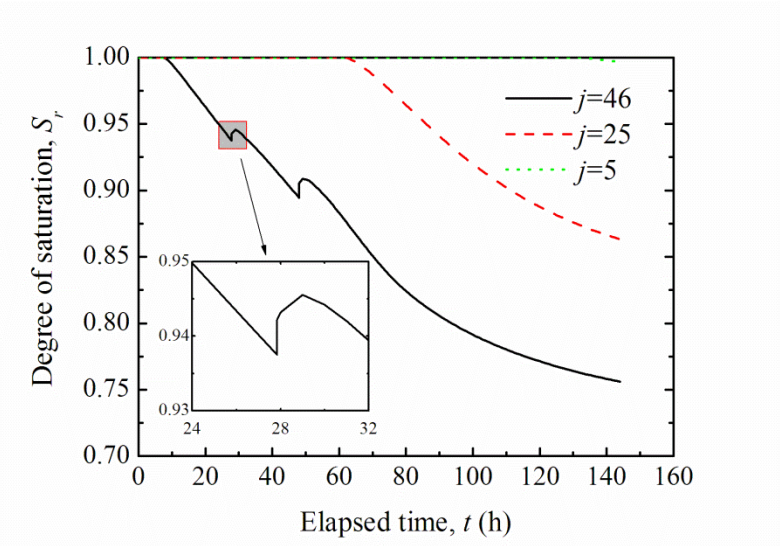

564

565 Figure 9 Results of (a) pore water pressure, (b) pore air pressure, and (c) the degree of
566 saturation, over elapsed time for locations at the top, middle and bottom of soil
567 column consolidated in test 2 of stepped loading.

568

569 In Figure 9a, the pore water pressures of the three elements are 12.5 kPa at the outset
570 and decrease in varied efficiencies. The most efficient occurs to element 46 and the
571 least to element 5. The pore water pressures in the three elements increase when the
572 additional loads are applied. The levels of increase however differ. Elements 5 and 25
573 echoes the load increments; element 46 however is not. The pore water pressure of
574 element 46 increases by 12.47 kPa in response to the 2nd load increment of 12.5 kPa
575 that is applied at t = 27.3 h, and by 17.9 kPa in response to the 3rd load increment of
576 25 kPa at t = 48 h. Both lead to Skempton's B-value less than 1, and the greater
577 elapsed time, the less the value. As opposed to Figure 9c, element 46 falls into its
578 unsaturated condition with S_r = 0.94 at t = 27.3 h and 0.9 at t = 48 h. Although the
579 values are often treated as nearly saturated, the volume of air of this element shares
580 parts of the load increment. The opposite occurs to elements 4 and 25 which are full

581 saturated when the loads are applied.

582

583 Similarly, element 46 develops its pore air pressure in a different pattern as opposed to
584 elements 5 and 25, as presented in Figure 9b. The pore air pressure starts at zero and
585 at t = 9 h becomes negative, suggesting the presence of pore air. The negative pressure
586 keeps decreasing until the 2nd load increment is applied. At the moment, the negative
587 pore air pressure changes to positive. The change is 8.57 kPa. It does not last long that
588 the positive pore air pressure drops to negative (due to the evolving negative pore
589 water pressure). Similar iterations occur when the 3rd load is applied. At the end of
590 consolidation, the pore air pressure dissipates completely as a result of additional
591 volume of air entering element 46. Elements 5 and 25 experience no air compression
592 as element 46 does. The two elements are saturated when the loads are applied.
593 Otherwise, similar iterations of pore air pressure (thus air compression) would occur.
594 The two elements become partially saturated after the loads application. Negative
595 pore air pressures are resulted, with the presence of greatest value of –16.8 kPa at
596 element 25 at t = 70 h. As with element 46, elements 5 and 25 tend to dissipate
597 respective negative pore air pressures at the late stage of consolidation.

598

599 The degrees of saturation of the three elements respond differently to the stepped
600 loading as presented in Figure 9c. At element 5, the degree of saturation remains unity
601 and is independent on the loading. Similar independence occurs to element 25, though
602 its degree of saturation decreases linearly with time since t = 61 h. The degree of

603 saturation at element 46 is influenced by the stepped loading. At the moments the
604 loads are applied, the degree of saturation increases instantaneously by a small value
605 (i.e., 0.005 to 0.01) and then, in a short period (e.g. 1 h), by another similarly small
606 value. The occurrence of first increment arises from the air compression, and the
607 second from the dissipation of positive pore air pressure. The latter is evidenced from
608 the pore air pressure coincidently dropping to zero as presented in Figure 9c.
609

610 **6. Conclusions**

611 This study presents model UEC2 developed for modelling electro-osmosis–surcharge
612 preloading combined consolidation of unsaturated soils. This model is a further step
613 to earlier series of models on electro-osmosis and is upgraded to simulate
614 one-dimensional consolidation of unsaturated soils where the electric field, hydraulic
615 flow and surcharge preloading coincide in directions. This model is validated against
616 experimental tests and applied to provide additional simulation results for the tests.
617 The research arrives at the following conclusions.

618 • Model UEC2 is able to account for electro-osmosis, hydraulic permeation, the
619 soil self-weight, and constitutive relationships. The constitutive relationships
620 include the soil compressibility, hydraulic conductivity, electro-osmotic
621 conductivity, air permeability and suction, and are based on the degree of
622 saturation. The model is open and can adopt any other constitutive
623 relationships. The algorithms used in the model account for nonlinear changes
624 of soil properties, the time-dependent loading and electric current, an external

625 hydraulic gradient, air compression, and varied degree of saturation of the soil
626 layer of interest.
627 • Model UEC2 provides the following quantities as a function of time: a) rate of
628 flow at the boundaries and b) the degree of consolidation of the soil layer. This
629 model also provides the following quantities as a function of time and location
630 within the soil layer: a) settlement, b) the void ratio, c) the pore water pressure,
631 d) the pore air pressure, e) the vertical effective stress, f) the moisture content,
632 and g) the electric potential and current density.
633 • The pore water pressure, pore air pressure and degree of saturation are
634 dependent on the elapsed time, depth, air permeability, water/air accessibility
635 and loading conditions. Over the elapsed time, the soil column becomes
636 unsaturated, progressing from the anode to the cathode. The closer to the
637 anode and the greater elapsed time, the more noticeable the unsaturated
638 condition (e.g., less S_r value) will be. The entry of air counteracts the
639 development of pore air pressure which eventually dissipates completely. A
640 portion of surcharge loads on unsaturated soils is borne by the volume of pore
641 air, resulting air compression and corresponding soil settlement. The
642 presumption of saturated conditions over-estimates soil settlement, as opposed
643 to the actual results in unsaturated conditions.
644 • Model UEC2 was developed in one-dimensional space where the electrodes
645 are horizontally orientated. This electrode set-up is applicable to many
646 post-filling scenarios, including the tailings or sludge disposal.

- The model parameters that are required for the permeability coefficients of unsaturated soils were determined indirectly and can be determined experimentally in the future.

Notations

The following symbols are used in this paper:

A_a	Element air volume
a_a	Parameter for pore air permeability
a_e	Parameter for electro-osmotic conductivity
a_v	Coefficient of compressibility
a_w	Parameter for hydraulic conductivity
b_a	Parameter for pore air permeability
b_e	Parameter for electro-osmotic conductivity
b_w	Parameter for hydraulic conductivity
C_c	Compression index
e	Void ratio
e_0	Initial void ratio
e_a	Pore air ratio
e_f	Final void ratio
G_s	Specific gravity of soil solids
H	Thickness of soil layer
H_0	Initial thickness of soil layer

669 h_w Total hydraulic head

670 h_a Total air head

671 h_{wt} Head at top boundary

672 h_{wb} Head at bottom boundary

673 i_e Voltage gradient, electric potential gradient

674 i_h Hydraulic gradient

675 i_a Pore air pressure gradient

676 j Element coordinate

677 k_a Pore air permeability

678 k_{as} Equivalent pore air permeability

679 k_d Pore air permeability in dry condition

680 k_e Electro-osmotic conductivity

681 k_{eo} Electro-osmotic conductivity in saturated condition

682 k_{es} Equivalent electro-osmotic conductivity

683 k_w Hydraulic conductivity

684 k_{wo} Hydraulic conductivity in saturated condition

685 k_{ws} Equivalent hydraulic conductivity

686 L_0 Initial height of element

687 L_j Height of element j

688 m Small number of settlement difference

689 m_{vG} Parameter of ven Genuchten model

690 n_{vG} Parameter of ven Genuchten model

691 p_a Atmosphere pressure

692 q_a Rate of pore air flow

693 q_e Rate of electro-osmotic flow

694 q_w Rate of hydraulic flow

695 q_0 Initial effective stress at top boundary

696 R_j Number of elements

697 R_k Number of data points for soil–water characteristic curve

698 R_l Number of data points for pore air permeability curve

699 R_m Number of data points for compressibility curve

700 R_n Number of data points for water permeability curves

701 S Settlement

702 S_e Effective degree of saturation

703 S_f Final settlement

704 S_r Degree of saturation

705 S_{rs} Residual degree of saturation

706 t Elapsed time of consolidation

707 t_f Final elapsed time of consolidation

708 U Degree of consolidation

709 u_a Pore air pressure

710 u_s Matric suction

711 u_{sb} Air-entry pressure

712 u_w Pore water pressure

713 V Electric potential difference

714 V_m Effective voltage

715 w Water content, moisture content

716 w_L Liquid limit

717 w_P Plastic limit

718 w_o Initial water content

719 z Vertical coordinate, elevation

720 α Constant used to determine the time step increment

721 α_{vG} Parameter of ven Genuchten model

722 γ Unit weight of soil

723 γ_a Unit weight of air

724 γ_w Unit weight of water

725 ρ Electrical resistivity

726 ρ_s Electrical resistivity of soil solids

727 ρ_w Electrical resistivity of pore fluid

728 σ Total vertical stress

729 σ' Effective vertical stress

730 χ Parameter in Bishop's model

731 Δe Void ratio increment

732 Δq Load increment

733 Δt Time step increment

734 **Superscripts**

735 i ith step of pore air compression

736 t Elapsed time of consolidation

737 ^ data points for compressibility curve

738 ¯ data points for water permeability curves

739 ˘ data points for pore air permeability curve

740 ~ data points for soil–water characteristic curve

741 **Subscripts**

742 j jth element

743 k kth data point for soil-water characteristic curve

744 l lth data point for pore air permeability curve

745 m mth data point for compressibility curve

746 n nth data point for water permeability curve

747 x representation for w, e, or a

748

749 **Acknowledgements**

750 This study was supported by the National Natural Science Foundation of China
751 (51608351) and the Natural Science Foundation of Tianjin (18JCYBJC22600).

752

753 **References**

754 [1] Deng A, Zhou YD. Modeling Electroosmosis and Surcharge Preloading
755 Consolidation. II: Validation and Simulation Results. J Geotech Geoenviron.
756 2016;142(4):04015094.

[2] Zhou YD, Deng A, Wang C. Finite-difference model for one-dimensional electro-osmotic consolidation. Comput Geotech. 2013;54(152–65.

[3] Lockhart NC. Electroosmotic dewatering of clays, III. Influence of clay type, exchangeable cations, and electrode materials. Colloids and Surfaces. 1983;6(3):253-69.

[4] Jeyakanthan V, Gnanendran CT, Lo SCR. Laboratory assessment of electro-osmotic stabilization of soft clay. Can Geotech J. 2011;48(12):1788-802.

[5] Jayasekera S. Electroosmotic and hydraulic flow rates through kaolinite and bentonite clays. Australian Geomechanics Journal. 2004;39(2):79-86.

[6] Esrig MI. Pore pressure, consolidation and electrokinetics. J Soil Mech Found Div. 1968;94(SM4):899–922.

[7] Hu L, Wu W, Wu H. Numerical model of electro-osmotic consolidation in clay. Geotechnique. 2012;62(6):537–41.

[8] Shang JQ. Electroosmosis-enhanced preloading consolidation via vertical drains. Can Geotech J. 1998;35(3):491–9.

[9] Wan TY, Mitchell JK. Electro-osmotic consolidation of soils. J Geotech Eng Div. 1976;102(5):473–91.

[10] Hu L, Wu H. Mathematical model of electro-osmotic consolidation for soft ground improvements. Geotechnique. 2014;64(2):155-64.

[11] Zhou YD, Deng A, Lu Q. A one-dimensional consolidation model considering large strain for unsaturated soil. Rock Soil Mechanics. 2018;39(5):1675–81.

[12] Casagrande L. Electro-osmosis in soils. Geotechnique. 1949;1(3):159–77.

779 [13] Wang L, Wang Y, Liu S, Fu Z, Shen C, Yuan W. Analytical solution for
780 one-dimensional vertical electro-osmotic drainage under unsaturated conditions.
781 Computers and Geotechnics. 2019;105(27-36.
782 [14] Townsend FC, Mcvay MC. SOA: Large Strain Consolidation Predictions. J
783 Geotech Eng-ASCE. 1990;116(2):222–43.
784 [15] Yuan J, Hicks MA. Influence of gas generation in electro-osmosis consolidation.
785 International Journal for Numerical and Analytical Methods in Geomechanics.
786 2016;40(11):1570-93.
787 [16] Zhou YD, Deng A, Liu ZX, Yang AW, Zhang H. One-dimensional electroosmosis
788 consolidation model considering variable saturation. Yantu Gongcheng
789 Xuebao/Chinese Journal of Geotechnical Engineering. 2017;39(8):1524-9.
790 [17] Fox PJ, Berles JD. CS2: A piecewise-linear model for large strain consolidation.
791 International Journal for Numerical and Analytical Methods in Geomechanics.
792 1997;21(7):453-75.
793 [18] Zhou Y, Deng A, Wang C. Finite-difference model for one-dimensional
794 electro-osmotic consolidation. Computers and Geotechnics. 2013;54(152-65.
795 [19] Deng A, Zhou Y. Modeling electroosmosis and surcharge preloading
796 consolidation. I: Model formulation. J Geotech Geoenviron. 2016;142(4).
797 [20] Mualem Y. A new model for predicting the hydraulic conductivity of unsaturated
798 porous media. Water Resour Res. 1976;12(3):513-22.
799 [21] Vogel T, van Genuchten MT, Cislerova M. Effect of the shape of the soil
800 hydraulic functions near saturation on variably-saturated flow predictions. Adv Water

801 Resour. 2000;24(2):133-44.
802 [22] Tamagnini C, Jommi C, Cattaneo F. A model for coupled
803 electro-hydro-mechanical processes in fine grained soils accounting for gas
804 generation and transport. Anais da Academia Brasileira de Ciencias.
805 2010;82(1):169-93.
806 [23] Amnyattalab J, Rezaie H. Study of the effect of seepage through the body of
807 earth dam on its stability by predicting the affecting hydraulic factors using models of
808 Brooks-Corey and van Genuchten (Case study of Nazluchay and Shahrchay earth
809 dams). Int J Environ Sci Te. 2018;15(12):2625-36.
810 [24] van Genuchten MT. Closed-form equation for predicting the hydraulic
811 conductivity of unsaturated soils. Soil Science Society of America Journal.
812 1980;44(5):892-8.
813 [25] Bishop A, Alpan I, Blight GE, Donald IB. Factors controlling the strength of
814 partly saturated cohesive soils. Proceedings of the Research Conference on Shear
815 Strength of Cohesive Soils. University of Colorado: ASCE, 1960. p. 503–32.
816 [26] Aitchison GD. Relationships of moisture stress and effective stress functions in
817 unsaturated soils. Pore Pressure and Suction in Soils. London: Butterworths, 1961. p.
818 47-52.
819 [27] Fredlund DG, Anqing X, Shangyan H. Predicting the permeability function for
820 unsaturated soils using the soil-water characteristic curve. Can Geotech J.
821 1994;31(4):533–46.
822 [28] Samouëlian A, Cousin I, Tabbagh A, Bruand A, Richard G. Electrical resistivity

823 survey in soil science: A review. Soil and Tillage Research. 2005;83(2):173-93.
824 [29] Komine H. Evaluation of chemical grouted soil by electrical resistivity.
825 Proceedings of the Institution of Civil Engineers - Ground Improvement.
826 1997;1(2):101-13.
827 [30] Gong XN, Jiao D, Li Y. Electric resistance calculation model of clay. Journal of
828 Shenyang University of Technology. 2011;33(2):312-218.
829 [31] Yin ZZ, Ling H. Simplified computation of ID consolidation for partially
830 saturated soil. Yantu Gongcheng Xuebao/Chinese Journal of Geotechnical
831 Engineering. 2007;29(5):633-7.
832